Guo, Z., et al., 2023, Disparate crustal thicknesses beneath oceanic transform faults and adjacent fracture zones revealed by gravity anomalies: Geology, https://doi.org/10.1130/G50429.1

Disparate crustal thicknesses beneath oceanic transform faults and adjacent fracture zones revealed by gravity anomalies

Zhikui Guo[1,2], Sibiao Liu[2], Lars Rüpke[2,*], Ingo Grevemeyer[2], Jason P. Morgan[3], Dietrich Lange[2], Yu Ren[2], and Chunhui Tao[1,4,*]

[1]*Key Laboratory of Submarine Geosciences, SOA, Second Institute of Oceanography, MNR, Hangzhou 310012, China*

[2]*GEOMAR, Helmholtz Centre for Ocean Research, Wischhofstrasse 1-3, 24148 Kiel*

[3]*Southern University of Science and Technology, Xueyuan Avenue 1088, 518055 Shenzhen*

[4]*School of Oceanography, Shanghai Jiao Tong University, 1954 Huashan Rd., Shanghai 200030, China*

[*]*lruepke@geomar.de, taochunhui@sio.org.cn*

SUPPLEMENTARY MATERIAL

1 Geodynamic simulations

We use the open-source code ASPECT version 2.1.0 (Bangerth et al., 2019) to develop 3-D geodynamic models with nonlinear viscoplastic rheology, following model setups similar to that in Grevemeyer et al. (2021). The steady-state simulations calculate the coupled thermo-mechanical evolution of ridge-transform systems, where the temperature field of the transform-fracture zone evolves dynamically in response to the prescribed surface spreading rate and the internal mantle flow.

In our models, the flow is driven by a kinematic, strike-slip boundary condition at the surface (Figure S1). The front and back sides have free-slip boundary conditions. Other boundary conditions (the left and right sides and the bottom) are set to the lithostatic pressure to allow free flow of material in and out. The temperatures at the top and bottom boundaries are fixed to 0°C and 1300°C, respectively. All other sides are insulated, i.e., no horizontal heat flux. The density varies with temperature: $\rho(T) = \rho_0[1 - \alpha(T - T_0)]$, where ρ_0 is the reference density at temperature T_0 and α is the volumetric thermal expansion coefficient (Table SS1).

The model resolution is 2.5 km/element in the ridge-transform area (0-10 km deep) and 10 km/element elsewhere. The geometry of the ridge-transform system and its spreading rate (Table SS2) are taken from the local bathymetric data (Grevemeyer et al., 2021) and the global topographic dataset of ETOPO1 (Amante and Eakins, 2009). The viscoplastic rheology contains a wet-olivine dislocation-creep viscosity (Hirth and Kohlstedt, 2003) and Drucker Prager plasticity (Table SS1). Further details on the viscoplastic setup and governing equations in ASPECT are provided elsewhere (e.g. Glerum et al., 2018;

Bangerth et al., 2019).

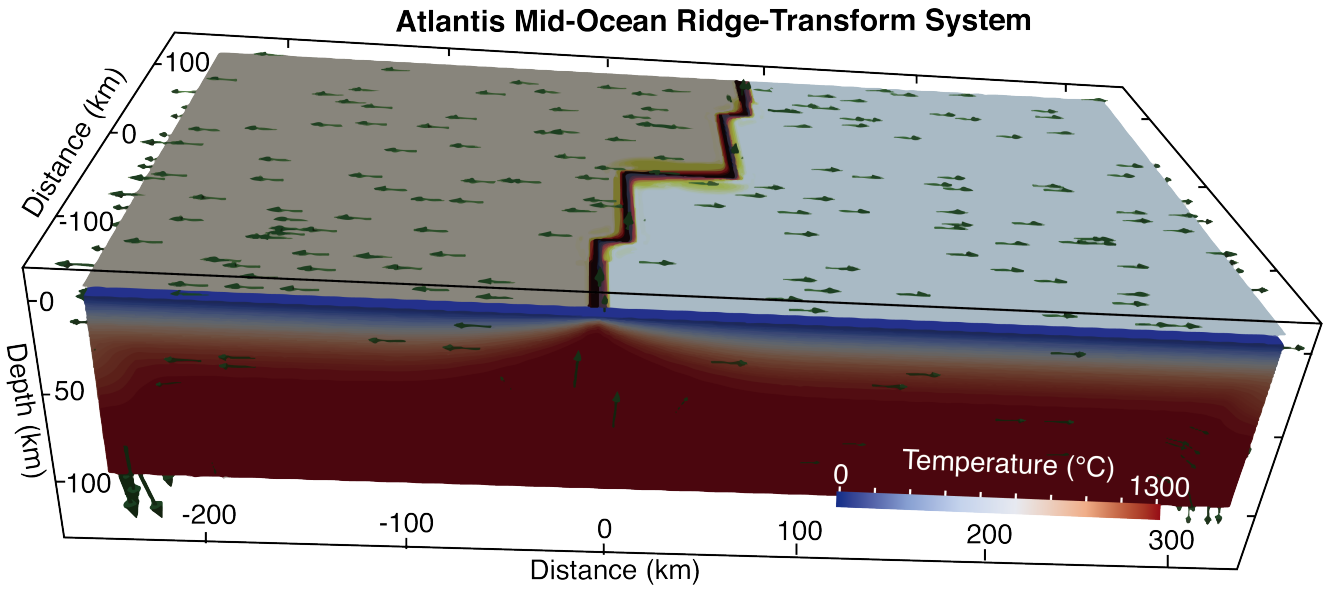

Figure S1. Model setup for the geodynamic simulation of the Atlantis transform example. The geometry of the mid-ocean ridge-transformation system (dark red) is extracted from bathymetric data Figure S3a. A kinematic boundary condition is imposed at the surface to simulate the Atlantis spreading, balanced by mantle upwelling from the open bottom boundary (green arrows).

2 Thermal corrections

The gravity correction (δg_T) of thermal effect is calculated from thermal-induced density anomalies estimated from 3-D geodynamic flow models. The density anomalies are calculated by $\delta\rho = \alpha\rho_0(T - T_0)$ and stored in an unstructured mesh consisting of cubic cells (see Figure S2). The gravity forward computing of such 3D density distribution is implemented in a C++ program named vtk2grav(Guo, 2022). For a specific cell C_i, it has a uniform density anomaly value $\delta\rho_i$ and the analytical solution(Nagy, 1966) of its gravity at point $P(x_j, y_j, z_j)$ can be expressed as follows,

$$\delta g_{T_i}(x_j,y_j,z_j) = G\delta\rho_i \left(x\ln(y+r) + y\ln(x+r) - z\arcsin\frac{z^2+y^2+yr}{(y+r)\sqrt{y^2+z^2}} \right) \Bigg|_{z_1-z_j}^{z_2-z_j} \Bigg|_{y_1-y_j}^{y_2-y_j} \Bigg|_{x_1-x_j}^{x_2-x_j} \tag{1}$$

where $r = \sqrt{x^2+y^2+z^2}$, $G = 6.67408 \times 10^{-11}\ m^3\ kg^{-1}\ s^{-2}$ is the gravitational constant. The notations $(x_1, x_2, y_1, y_2, z_1, z_2)$ of coordinates of cell C_i are shown in Figure S2. Therefore, the thermal correction at point $P(x_j, y_j, z_j)$, which is the same as the data points of the mantle Bouguer anomaly map, can be calculated as,

Table S1. Parameters used in the geodynamic model and RMBA calculation.

Parameter	Value
Sea water density ($kg\ m^{-3}$)	1030
Reference crustal density ($kg\ m^{-3}$)	2700
Reference mantle density, ρ_0 ($kg\ m^{-3}$)	3300
Reference crustal thickness (km)	6
Reference temperature, T_0 (°C)	1300
Thermal expansion, α (1/K)	3.5e-5
Thermal conductivity ($WK^{-1}m^{-1}$)	3.0
Heat capacity ($Jkg^{-1}K^{-1}$)	1250
Activation volume for dislocation creep (cm^3mol^{-1})	22
Activation energy for dislocation creep (kJmol^{-1})	520
Prefactor for dislocation creep ($Pa^{-n}s^{-1}$)	3.6e-14
Stress exponent for dislocation creep	3.5
Frictional angle (°)	30
Cohesions (MPa)	10

$$\delta g_T(x_j,y_j,z_j) = \sum_{i=1}^{N} \delta g_{Ti}(x_j,y_j,z_j) \tag{2}$$

where N is the cell number of the 3D geodynamic model result.

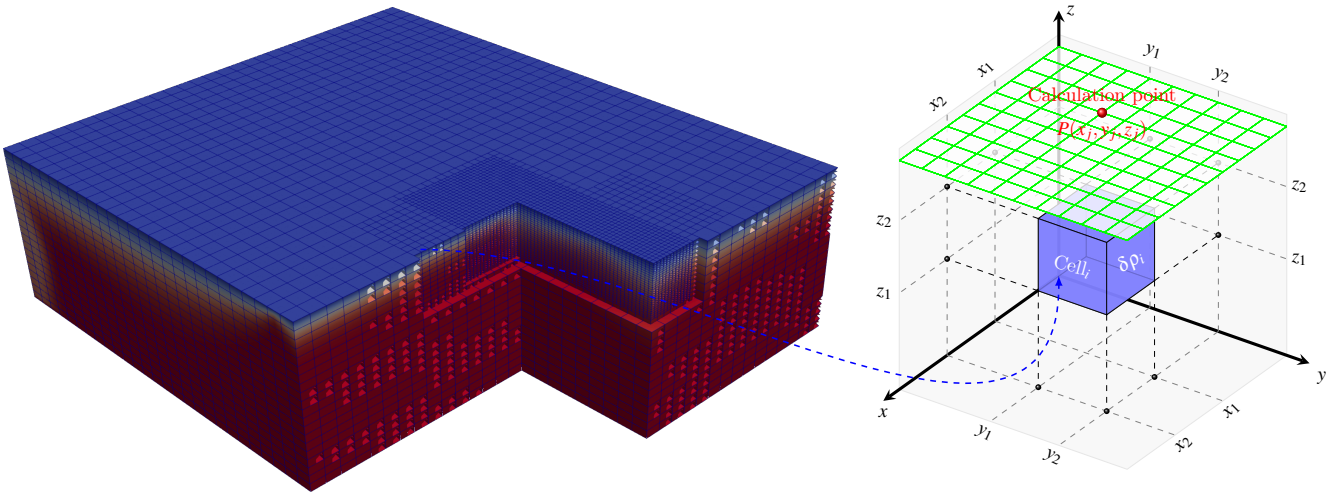

Figure S2. Mesh of the 3D thermal model result (left) and notation used for gravity forward of a cubic body (right). $x_1, x_2, y_1, y_2, z_1, z_2$ are the coordinates of six corner point of the cubic body (transparent blue box with black edges). $P(x_j,y_j,z_j)$ represent the gravity forward calculation point and the greenish grid represents data points of the MBA map (e.g. Figure S3b) which requires thermal correction.

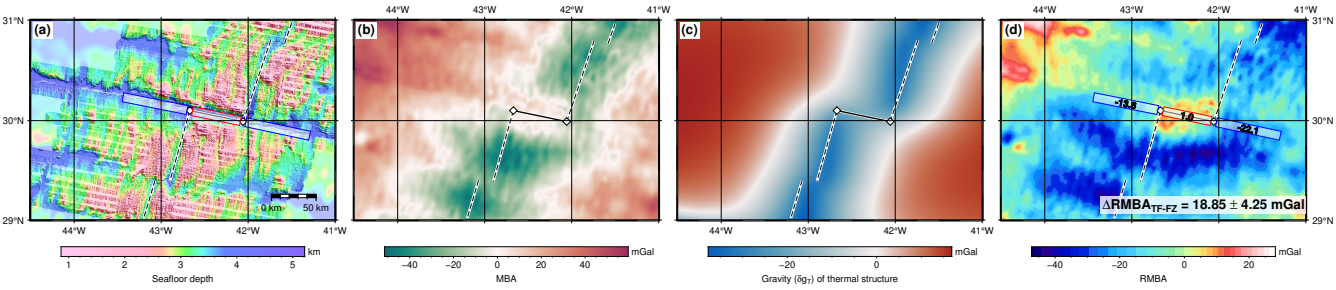

Figure S3. Input data and results of the Atlantis transform fault offsetting the Mid-Atlantic Ridge. (a) Bathymetric map; (b) Mantle Bouguer Anomaly (MBA); (c) gravitational effect of the lithospheric thermal structure; (d) Residual Mantle Bouguer Anomaly (RMBA). Symbols and lines as in Figure 2

.

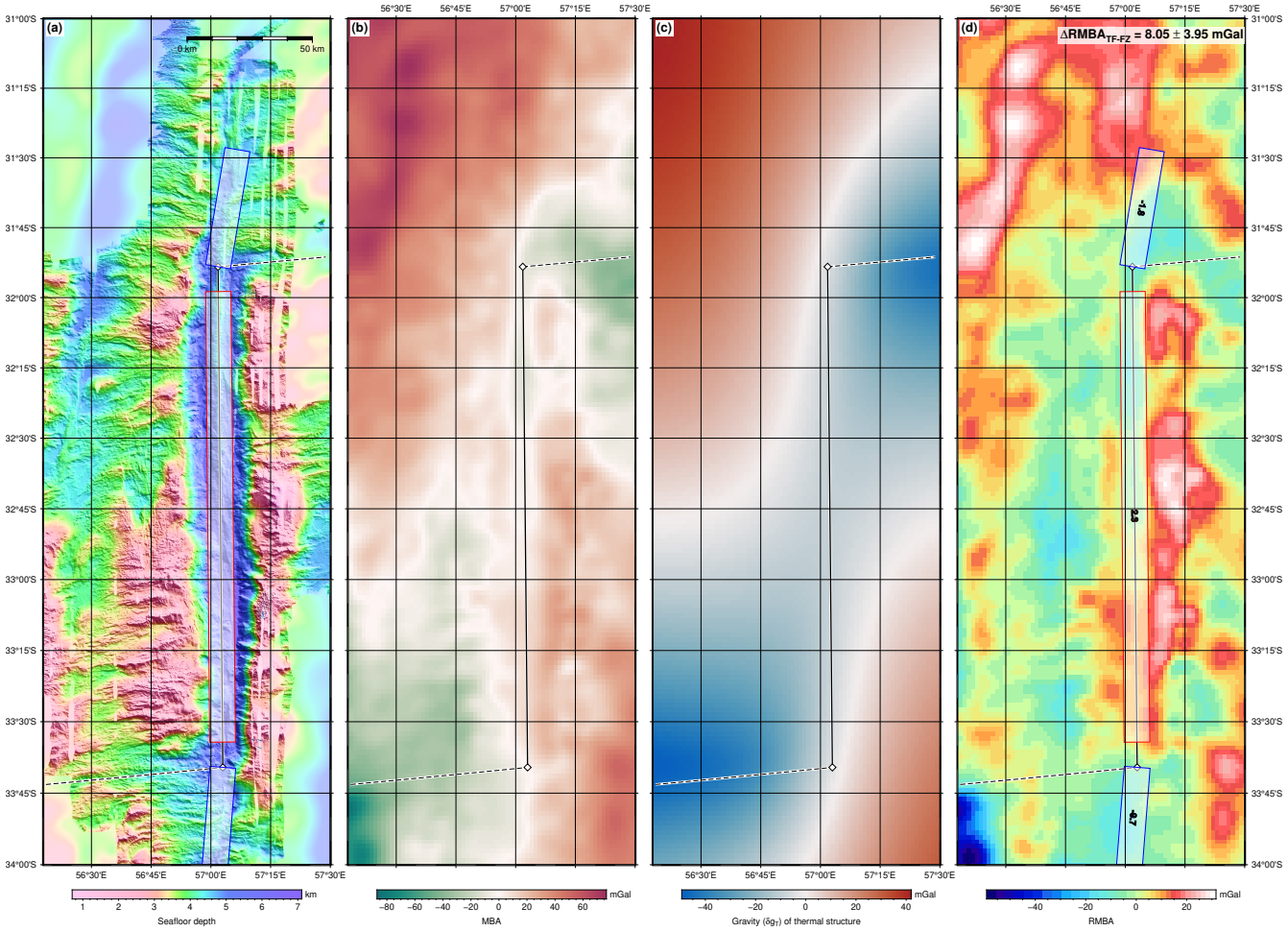

Figure S4. Input data and results of the Atlantis II transform fault offsetting the Southwest Indian Ridge. (a) Bathymetric map; (b) Mantle Bouguer Anomaly (MBA); (c) gravitational effect of the lithospheric thermal structure; (d) Residual Mantle Bouguer Anomaly (RMBA). Symbols and lines as in Figure 2.

.

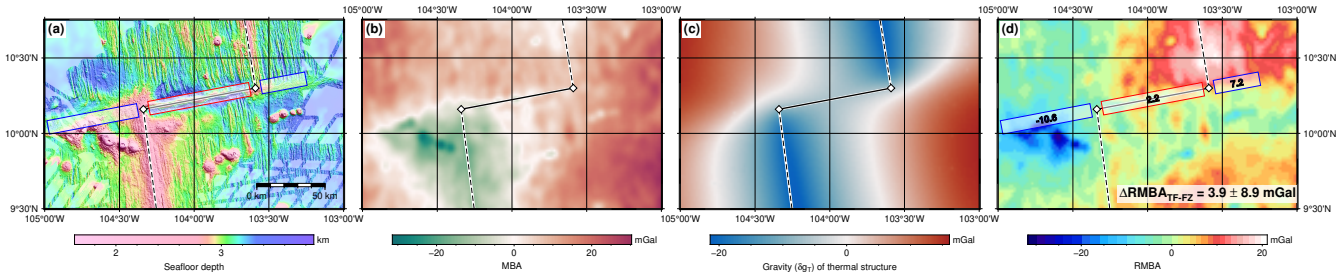

Figure S5. Input data and results of the Clipperton transform fault offsetting the East Pacific Rise. (a) Bathymetric map; (b) Mantle Bouguer Anomaly (MBA); (c) gravitational effect of the lithospheric thermal structure; (d) Residual Mantle Bouguer Anomaly (RMBA). Symbols and lines as in Figure 2.

.

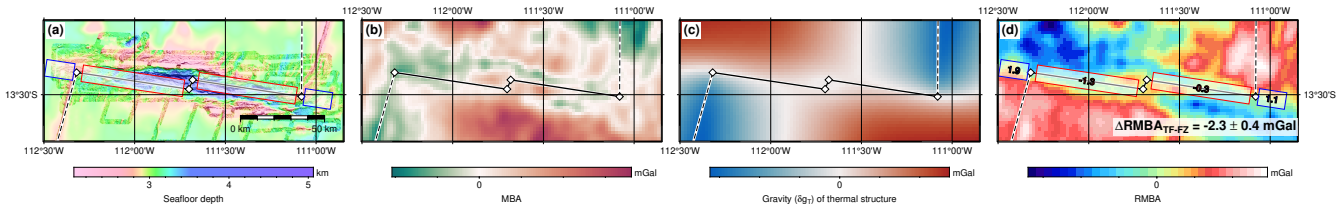

Figure S6. Input data and results of the Garrett transform fault offsetting the East Pacific Rise. (a) Bathymetric map; (b) Mantle Bouguer Anomaly (MBA); (c) gravitational effect of the lithospheric thermal structure; (d) Residual Mantle Bouguer Anomaly (RMBA). Symbols and lines as in Figure 2.

.

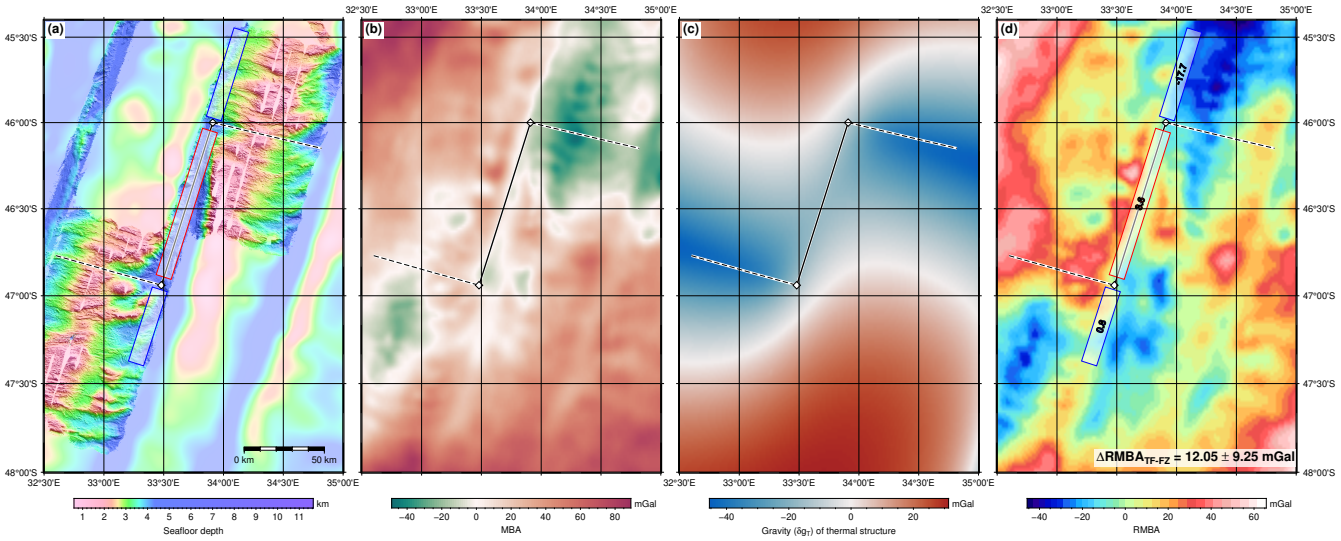

Figure S7. Input data and results of the Marion transform fault offsetting the Southwest Indian Ridge. (a) Bathymetric map; (b) Mantle Bouguer Anomaly (MBA); (c) gravitational effect of the lithospheric thermal structure; (d) Residual Mantle Bouguer Anomaly (RMBA). Symbols and lines as in Figure 2.

.

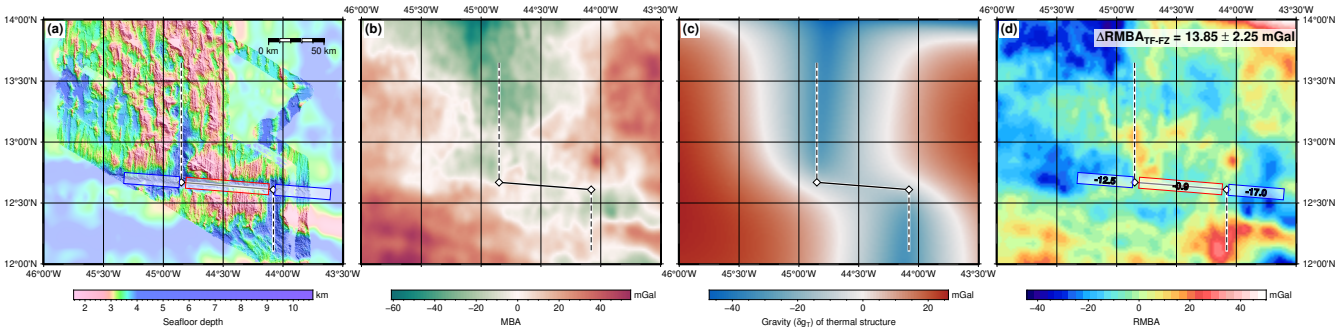

Figure S8. Input data and results of the Marathon transform fault offsetting the Mid-Atlantic Ridge. (a) Bathymetric map; (b) Mantle Bouguer Anomaly (MBA); (c) gravitational effect of the lithospheric thermal structure; (d) Residual Mantle Bouguer Anomaly (RMBA). Symbols and lines as in Figure 2.

.

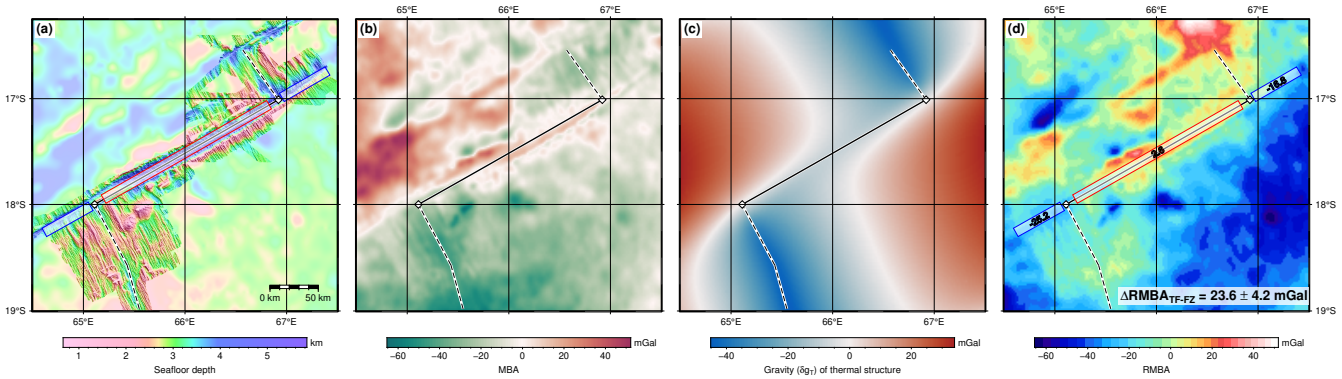

Figure S9. Input data and results of the Marie Celester transform fault offsetting the Central Indian Ridge. (a) Bathymetric map; (b) Mantle Bouguer Anomaly (MBA); (c) gravitational effect of the lithospheric thermal structure; (d) Residual Mantle Bouguer Anomaly (RMBA). Symbols and lines as in Figure 2.

.

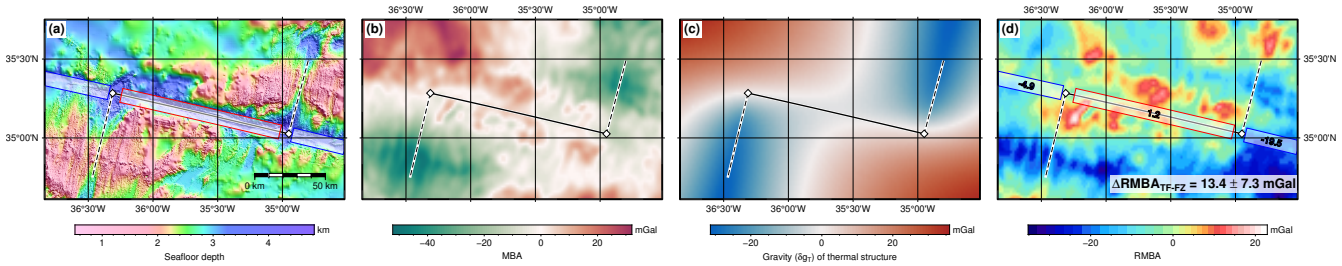

Figure S10. Input data and results of the Oceanographer transform fault offsetting the Mid-Atlantic Ridge. (a) Bathymetric map; (b) Mantle Bouguer Anomaly (MBA); (c) gravitational effect of the lithospheric thermal structure; (d) Residual Mantle Bouguer Anomaly (RMBA). Symbols and lines as in Figure 2.

.

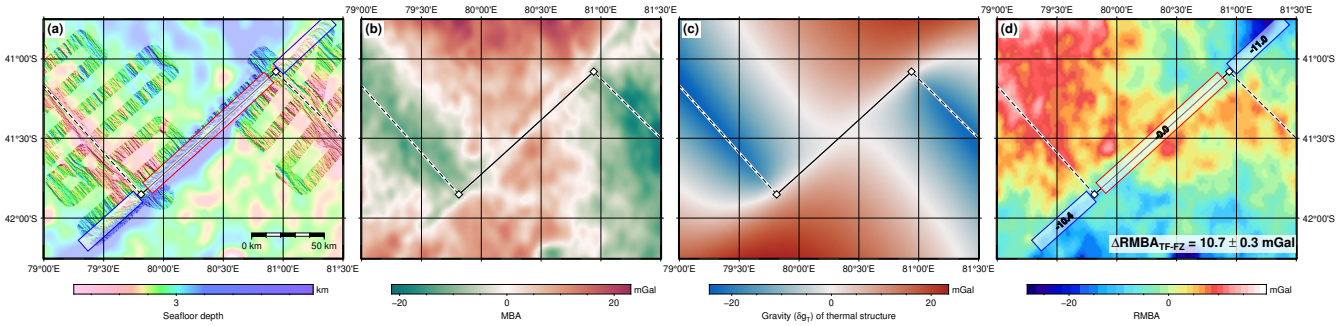

Figure S11. Input data and results of the Vlamingh transform fault offsetting the Southeast Indian Ridge. (a) Bathymetric map; (b) Mantle Bouguer Anomaly (MBA); (c) gravitational effect of the lithospheric thermal structure; (d) Residual Mantle Bouguer Anomaly (RMBA). Symbols and lines as in Figure 2.

.

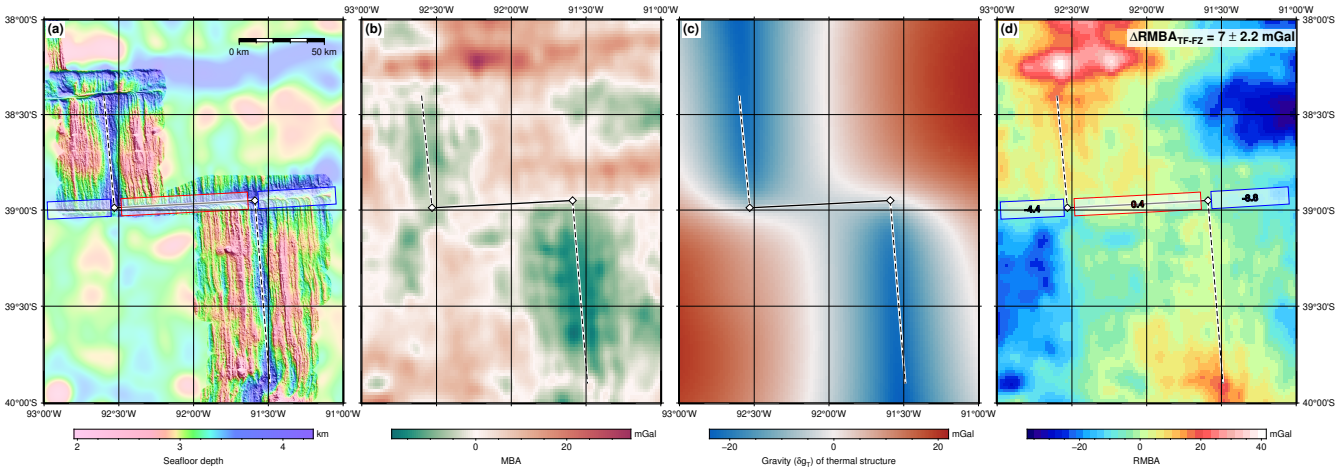

Figure S12. Input data and results of the CR-TF 39°S transform fault offsetting the Chile Ridge. (a) Bathymetric map; (b) Mantle Bouguer Anomaly (MBA); (c) gravitational effect of the lithospheric thermal structure; (d) Residual Mantle Bouguer Anomaly (RMBA). Symbols and lines as in Figure 2.

.

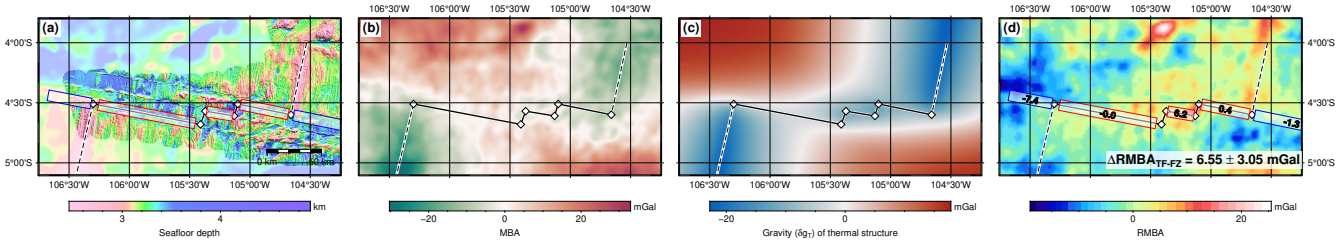

Figure S13. Input data and results of the Gofar transform fault offsetting the East Pacific Rise. (a) Bathymetric map; (b) Mantle Bouguer Anomaly (MBA); (c) gravitational effect of the lithospheric thermal structure; (d) Residual Mantle Bouguer Anomaly (RMBA). Symbols and lines as in Figure 2.

.

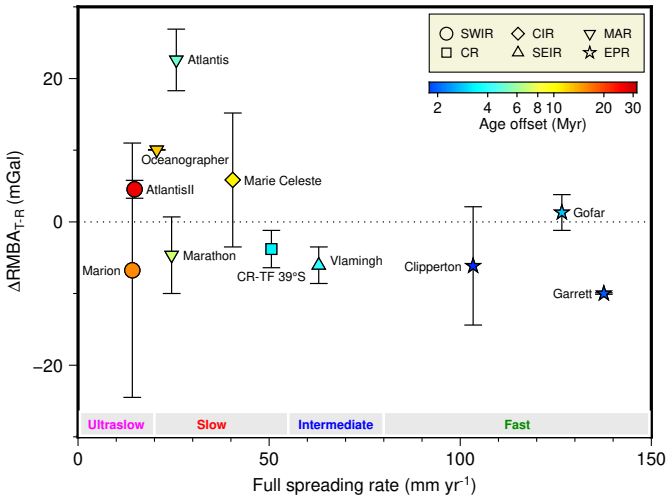

Figure S14. Variation of ΔRMBA$_{T\text{-}R}$ as a function of spreading rate. ΔRMBA$_{T\text{-}R}$—mean difference of RMBA between transform fault and associated ridge segments. Associated spreading ridge of each transform fault is indicated by different symbols. SWIR (circle)—Southwest Indian Ridge; CIR (diamond)—Central Indian Ridge; MAR (inverted triangle)—Mid-Atlantic Ridge; CR-TF 39°S (square)—Transform fault near 39°S offsetting the Chile Ridge; SEIR (triangle)—Southeast Indian Ridge; EPR (star)—East Pacific Rise. The with of average box along ridge segments is 20 km which is consistent with that in Gregg et al. (2007).

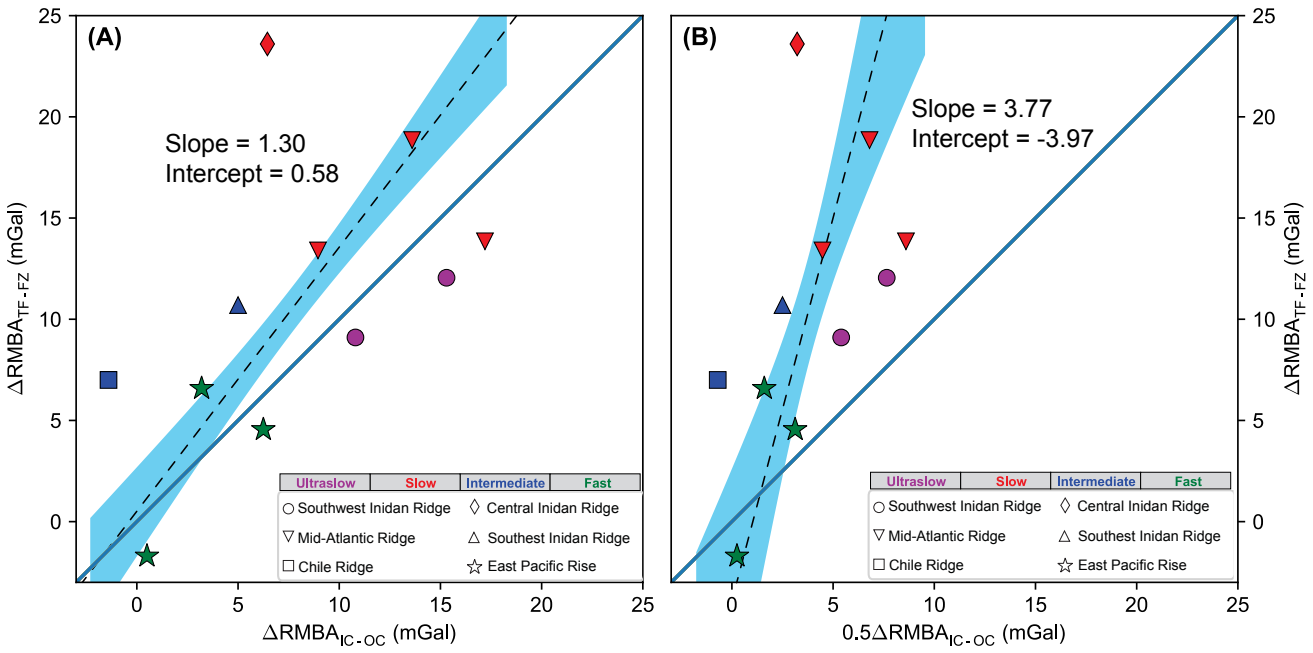

Figure S15. Correlation between $\Delta RMBA_{TF-FZ}$ and $\Delta RMBA_{IC-OC}$. (A) $\Delta RMBA_{TF-FZ}$ versus $\Delta RMBA_{IC-OC}$. (B) $\Delta RMBA_{TF-FZ}$ versus $0.5\Delta RMBA_{IC-OC}$. The blue line indicates equal gravity. Dashed line represents linear regression, and the blue-shaded region denotes the 95% confidence region.

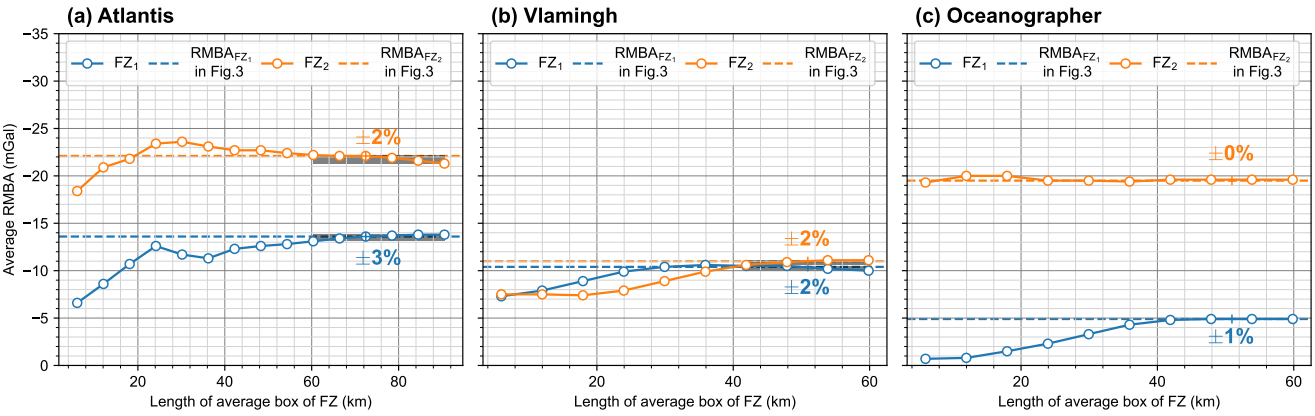

Figure S16. Average RMBA calculation in FZs is started from a small box with length 6 km, then incrementally (interval is 6 km) increase the box length to the maximum length of high-resolution bathymetry coverage. These tests are done for (a) Atlantis, (b) Vlamingh and (c) Oceanographer with significant lateral extents of FZ bathymetry. The solid lines with circle markers represent average RMBA of FZ changes with length of average box. The dashed lines represent the average RMBA value of FZs used in our main result in the main text (e.g. Figure 3)

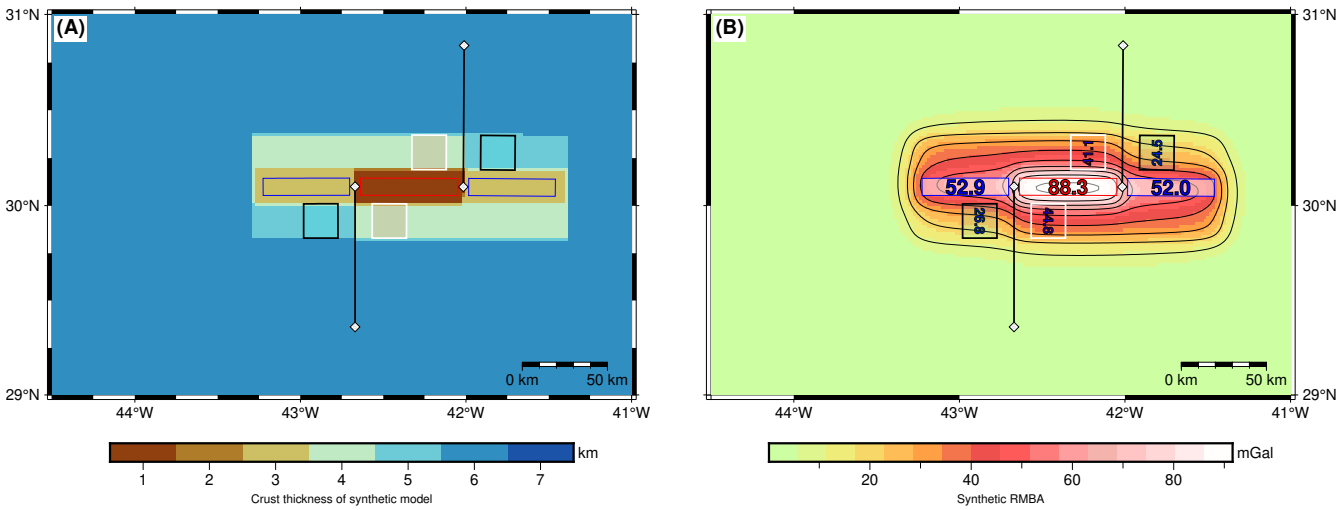

Figure S17. Example of Synthetic model. (A) Synthetic crustal thickness with IC=3 km, OC = 5km, TF = 1 1km, FZ = 3 km, and the normal crust thickness is 6 km. (B) RMBA due to the crustal structure shown in (A). The density of crust and mantle are listed in Table S1. The red box denotes the average region of transform fault. The blue, black and white boxes denote the average region of fracture zones, outside corners and inside corners, respectively. The number in each box in figure (B) shows the average RMBA value. Black lines with diamond marker show the ridges and RTIs.

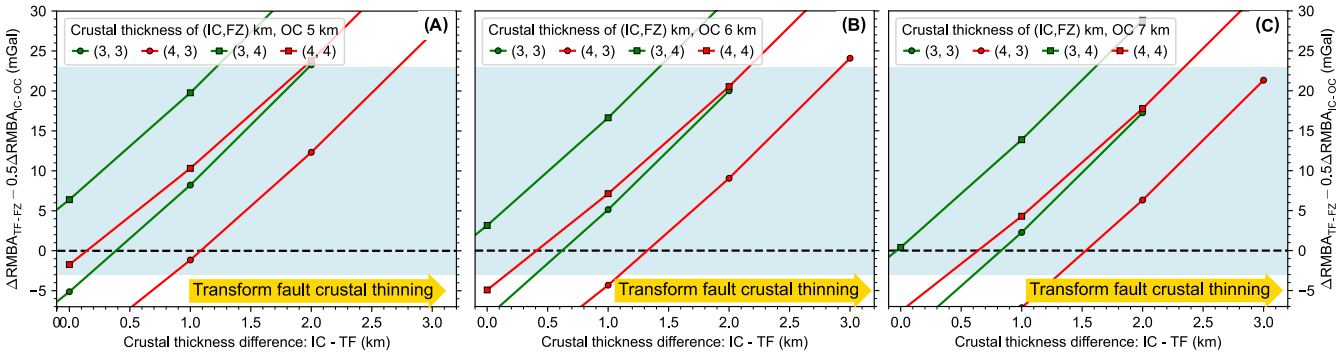

Figure S18. $\Delta RMBA_{TF-FZ} - \Delta RMBA_{IC-OC}$ **of synthetic models with different combinations of crustal thickness of IC, TF, FZ.** (A), (B) and (C) represent synthetic model group with crust thickness of OC 5 km, 6 km and 7 km, respectively. Each data point represent result of a synthetic model (see Figure S17) with specific combination of crustal thickness of IC, FZ, OC (see legend) and FZ. The positive direction of x-axis means transform fault crust thinning relative to inside corner. The light blue area represent $\Delta RMBA_{TF-FZ} - \Delta RMBA_{IC-OC}$ range of observation data (see Figure 3 in the main text).

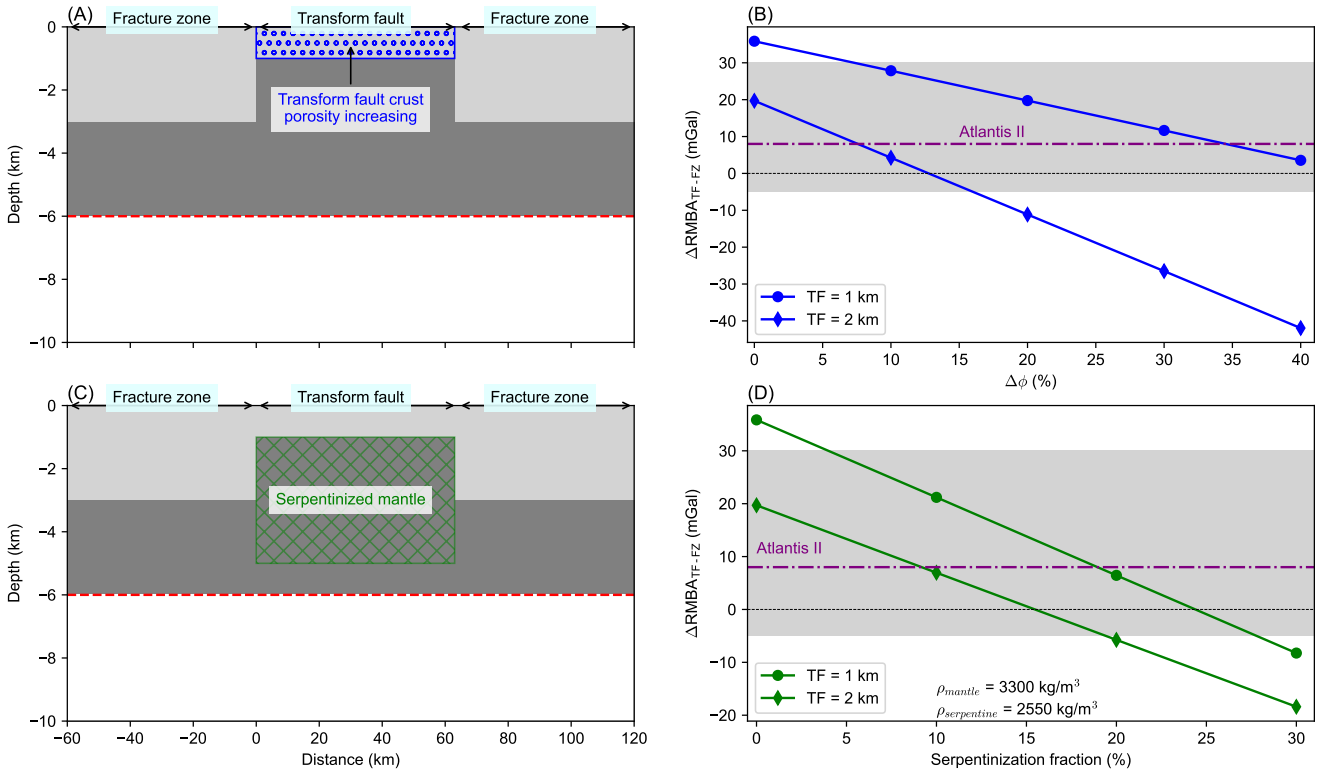

Figure S19. Synthetic model result of the gravity effect of crustal porosity increasing and mantle serpentinization underneath transform fault. (A) shows the geometry of fracture-transform-fracture profile and where is the crustal porosity increasing. (B) $\Delta RMBA_{TF-FZ}$ as a function of porosity increasing in transform fault crust. (C) shows where is the serpentinized mantle. (D) shows $\Delta RMBA_{TF-FZ}$ as a function of serpentinization fraction. Legends in (C) and (D) represent two models with TF crustal thickness 1 km, 2km and 2.5 km, respectively. The map view of the crustal structure of the synthetic model is shown in Figure S17A.

Table S2. Transform fault characteristics used in this study.

Transform fault	Latitude (°N)	Longitude (°E)	Spreading rate (mm yr^{-1})	Age offset (Myr)	$\Delta RMBA_{OTF\text{-}FZ}$ (mGal)	$\Delta RMBA_{IC\text{-}OC}$ (mGal)	Reference
Atlantis	30.05	-42.32	25.7	4.90	18.85	13.60	Figure S3
Atlantis II	-32.78	57.07	14.8	26.45	9.10	10.80	Figure S4
Clipperton	10.22	-103.93	103.4	1.62	4.55	6.25	Figure S5
Garrett	-13.40	-111.50	137.6	1.95	-1.70	0.50	Figure S6
Marion	-46.45	33.72	14.2	15.49	12.05	15.29	Figure S7
Marathon	12.65	-44.50	24.5	6.94	13.85	17.2	Figure S8
Marie Celester	-17.51	66.00	40.5	10.91	23.6	6.45	Figure S9
Oceanographer	35.25	-35.60	20.6	12.33	13.40	8.95	Figure S10
Vlamingh	-41.47	80.36	63	4.03	10.70	5.00	Figure S11
CR-TF 39°S	-38.97	-92.05	50.6	3.24	7.00	-1.40	Figure S12
Gofar	-4.60	-105.85	126.6	2.81	6.58	3.20	Figure S13

SUPPLEMENTARY REFERENCES

Amante, C. and Eakins, B. W.: ETOPO1 arc-minute global relief model: procedures, data sources and analysis, https://doi.org/10.7289/V5C8276M, 2009.

Bangerth, W., Dannberg, J., Gassmoeller, R., and Heister, T.: ASPECT v2.1.0, https://doi.org/10.5281/zenodo.2653531, 2019.

Glerum, A., Thieulot, C., Fraters, M., Blom, C., and Spakman, W., 2018, Nonlinear viscoplasticity in ASPECT: benchmarking and applications to subduction: Solid Earth, 9, 267–294, https://doi.org/10.5194/se-9-267-2018.

Gregg, P. M., Lin, J., Behn, M. D., and Montési, L. G., 2007, Spreading rate dependence of gravity anomalies along oceanic transform faults: Nature, 448, 183–187, https://doi.org/10.1038/nature05962.

Grevemeyer, I., Rüpke, L. H., Morgan, J. P., Iyer, K., and Devey, C. W., 2021, Extensional tectonics and two-stage crustal accretion at oceanic transform faults: Nature, 591, 402–407, https://doi.org/10.1038/s41586-021-03278-9.

Guo, Z.: vtk2grav: A computer program for gravity forward of 3D density distribution in VTK format, https://doi.org/10.5281/zenodo.5831568, URL `https://doi.org/10.5281/zenodo.5831568`, 2022.

Hirth, G. and Kohlstedt, D., 2003, Rheology of the upper mantle and the mantle wedge: A view from the experimentalists: Washington DC American Geophysical Union Geophysical Monograph Series, 138, 83–105, https://doi.org/10.1029/138GM06.

Nagy, D., 1966, The gravitational attraction of a right rectangular prism: Geophysics, 31, 362–371, https://doi.org/10.1190/1.1439779.